

# Chaotic Lagrangian transport and mixing in the ocean

S.V. Prants

Laboratory of Nonlinear Dynamical Systems,  
Pacific Oceanological Institute of the Russian Academy of Sciences,  
43 Baltiiskaya st., 690041 Vladivostok, Russia,  
prants@poi.dvo.ru, URL: <http://dynalab.poi.dvo.ru>

## Abstract

Dynamical systems theory approach has been successfully used in physical oceanography for the last two decades to study mixing and transport of water masses in the ocean. The basic theoretical ideas have been borrowed from the phenomenon of chaotic advection in fluids, an analogue of dynamical Hamiltonian chaos in mechanics. The starting point for analysis is a velocity field obtained by this or that way. Being motivated by successful applications of that approach to simplified analytic models of geophysical fluid flows, researchers now work with satellite-derived velocity fields and outputs of sophisticated numerical models of ocean circulation. This review article gives an introduction to some of the basic concepts and methods used to study chaotic mixing and transport in the ocean and a brief overview of recent results with some practical applications of Lagrangian tools to monitor spreading of Fukushima-derived radionuclides in the ocean.

## 1 Chaotic advection in fluids: from lab to geophysical flows

It is well known that dynamical chaos may occur in simple deterministic mechanical systems. One-dimensional physical pendulum under the influence of a periodic force can move strictly periodically under some initial conditions and is able to rotate irregularly under another ones. Roughly speaking, dynamical chaos means that a distance between initially nearby trajectories in the phase space grows exponentially in time

$$\|\delta\vec{r}(t)\| = \|\delta\vec{r}(0)\|e^{\lambda t}, \quad (1)$$

where  $\lambda$  is a positive number, known as the maximal Lyapunov exponent, which characterizes asymptotically (at  $t \rightarrow \infty$ ) the average rate of that separation, and  $\|\cdot\|$  is a norm of the position vector  $\vec{r}$ . It immediately follows from (1) that nobody able to forecast the pendulum position  $x$  beyond the so-called predictability horizon

$$T_{\text{pred}} \simeq \frac{1}{\lambda} \ln \frac{\|\Delta_x\|}{\|\Delta_x(0)\|}, \quad (2)$$

where  $\|\Delta_x\|$  is a confidence interval and  $\|\Delta_x(0)\|$  is a practically inevitable inaccuracy in specifying pendulum's initial position. The deterministic dynamical system with positive maximal Lyapunov exponents for almost all initial positions and momenta (in the sense of nonzero measure) is called fully chaotic. The phase space of a typical chaotic Hamiltonian system contains islands of regular motion embedded in a stochastic sea. The dependence of the predictability horizon  $T_{\text{pred}}$  on the lack of our knowledge of exact location is logarithmic, i.e., it is much weaker than on the measure of dynamical instability quantified by  $\lambda$ . Simply speaking, with any reasonable degree of accuracy on specifying initial conditions there is a

time interval beyond which the forecast is impossible, and that time may be rather small for chaotic systems. It is the ultimate reason why the exact weather forecast is impossible no matter how perfect detectors for measuring initial parameters and how powerful computers we have got.

## 1.1 What is chaotic advection

Methods of theory of dynamical systems have been actively used in the last 30 years to describe advection of passive particles in fluid flows on a large range of scales, from microfluidic flows to ocean and atmospheric ones. If advected particles rapidly adjust their own velocity to that of a background flow and do not affect the flow properties, then they are called passive and satisfy simple equations of motion

$$\frac{d\mathbf{r}}{dt} = \mathbf{v}(\mathbf{r}, t), \quad (3)$$

where  $\mathbf{r} = (x, y, z)$  and  $\mathbf{v} = (u, v, w)$  are the position and velocity vectors at a point  $(x, y, z)$ . This formula just means that the Lagrangian velocity of a passive particle (the left side of Eq. (3)) equals to the Eulerian velocity of the flow at the location of that particle (the right side of Eq. (3)). In fluid mechanics by passive particles one means water (air) small parcels with their properties or small foreign bodies in a flow. If the Eulerian velocity field is supposed to be regular, the vector equation (3) in nontrivial cases is a set of three nonlinear deterministic differential equations whose phase space is a physical space for advected particles. Solutions of those equations can be chaotic in the sense of exponential sensitivity to small variations in initial conditions and/or control parameters as in Eq. (1).

As to advection equations, it was Arnold [1] who firstly suggested chaos in the field lines (and, therefore, in trajectories) for a special class of three-dimensional stationary flows (so-called ABC flows), and this suggestion has been confirmed numerically by Hénon [2]. The term “chaotic advection” has been coined by Aref [3,4] who realized that advection equations for two-dimensional flows may have a Hamiltonian form. For incompressible planar flows, the velocity components can be expressed in terms of a streamfunction. The equations of motion (3) have now the Hamiltonian form

$$\frac{dx}{dt} = u(x, y, t) = -\frac{\partial \Psi}{\partial y}, \quad \frac{dy}{dt} = v(x, y, t) = \frac{\partial \Psi}{\partial x}, \quad (4)$$

with the streamfunction  $\Psi$  playing the role of a Hamiltonian. The coordinates  $(x, y)$  of a particle are canonically conjugated variables. All time-independent one-degree-of-freedom Hamiltonian systems are known to be integrable. It means that all fluid particles move along streamlines of a time-independent streamfunction in a regular way. Equations (4) with a time-periodic streamfunction are usually non-integrable, giving rise to chaotic particle’s trajectories. Chaotic advection has been studied both analytically and numerically in a number of simple models with point vortices and in laboratory experiments [4, 5].

Since the phase plane of the 2D dynamical system (4) is the physical space for fluid particles, many abstract mathematical objects from dynamical systems theory (stagnation points, KAM tori, stable and unstable manifolds, periodic and chaotic orbits, etc.) have their material analogues in fluid flows. It is well known that besides “trivial” elliptic stagnation points (ESP), the motion around which is stable, there are hyperbolic stagnation points (HSP) which organize fluid motion in their neighborhood in a specific way. In a steady flow the hyperbolic points are typically connected by the separatrices which are their stable and unstable invariant manifolds (Fig. 1a). In a time-periodic flow they are replaced by the corresponding hyperbolic trajectories (HTs) with two associated invariant manifolds which in general intersect each other transversally (Fig. 1b) resulting in a complex manifold structure known as homo- or heteroclinic tangles. The fluid motion in these regions is so complicated that it may be strictly called chaotic, the phenomenon known as chaotic advection. Initially close fluid particles in such tangles rapidly diverge providing very effective mechanism for mixing. The phase space of a typical chaotic open flow consists of different kinds of invariant

sets — KAM tori with regular trajectories of fluid particles, cantori and a chaotic saddle set — embedded into a stochastic sea with chaotic trajectories (see, e.g., Refs. [6, 7] where it is illustrated with a simple open flow).

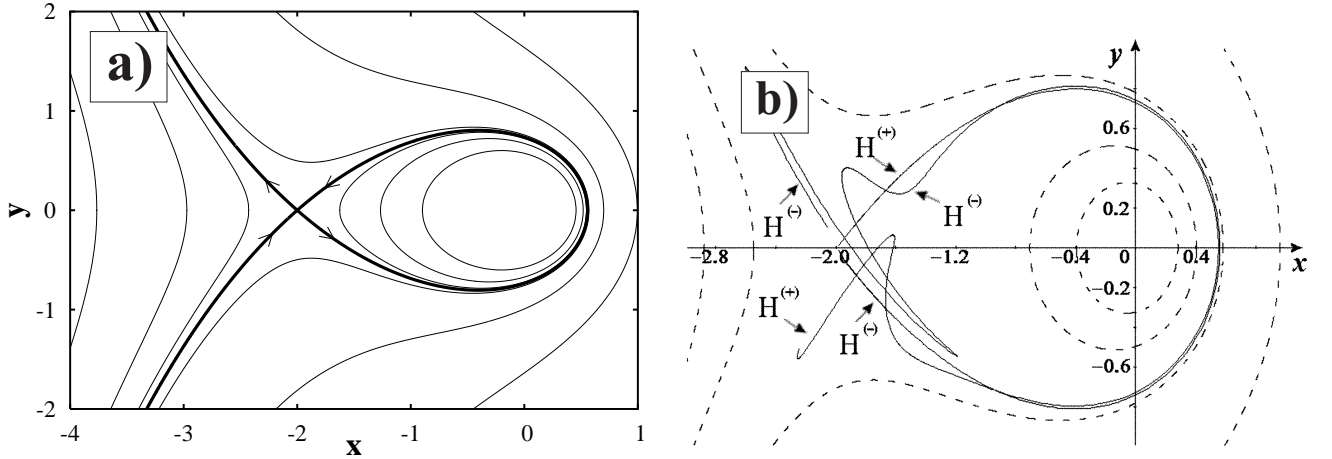


Figure 1: a) A steady flow with the HSP whose stable and unstable manifolds coincide forming a closed separatrix. b) Under a perturbation the HSP becomes a hyperbolic trajectory with intersecting stable  $H^{(+)}$  and unstable  $H^{(-)}$  manifolds. The stochastic layer around the unperturbed separatrix is a seed of Hamiltonian chaos.

Stable and unstable manifolds are important organizing structures in the flow because they attract and repel fluid particles not belonging to them and partition the flow into regions with distinct regimes of motion. Invariant manifold in a 2D flow is a material line, i. e., it is composed of the same fluid particles in course of time. By definition, stable,  $H^{(+)}$ , and unstable,  $H^{(-)}$ , manifolds of a hyperbolic trajectory  $\gamma(t)$  are material lines consisting of a set of points through which at time moment  $t$  pass trajectories asymptotical to  $\gamma(t)$  at  $t \rightarrow \infty$  ( $H^{(+)}$ ) and  $t \rightarrow -\infty$  ( $H^{(-)}$ ). They are complicated curves infinite in time and space (in theory) that act as barriers to fluid transport (see, e.g., [8, 9]).

## 1.2 Chaotic advection in analytic models of geophysical flows

The famous paradigm of dissipative dynamical chaos, the Lorenz attractor, appeared as a toy model of atmospheric circulation. The first examples of Hamiltonian dynamical chaos in the ocean have been reviewed in [10] for describing sound propagation in so-called underwater sound channels in the ocean where acoustic waves can propagate over long distances practically without losses [11] (for recent reviews on ray and wave chaos in underwater acoustics see [12, 13]).

The present article focuses on some advances in describing Lagrangian transport and mixing in the ocean that have been made for 2D flows. The assumption that the motion is two-dimensional is justified partly by the fact that typically horizontal velocities in the ocean are much larger than the vertical ones, by four orders of magnitude ( $10^{-1}$  vs  $10^{-5}$  m/s). 2D flows are particularly relevant for studies of pollution transport and other processes on the ocean surface. However, 2D analysis should be applied with caution if one study transport and mixing in the areas with strong upwelling where vertical velocities may be comparable with the horizontal ones.

Kinematics of an incompressible 2D fluid flow is described by a streamfunction  $\Psi$  which gives a complete description of the velocity field through Eq.(4). If the streamfunction is specified without any respect to laws of fluid motion, then the model is said to be kinematic. The simplest analytic models of chaotic advection in the ocean are kinematic. In fact, kinematic streamfunctions are constructed “by hands” based on some heuristic assumptions. If the streamfunction satisfies to one of the governing equations of fluid motion, the corresponding models are called dynamical ones. In spite of simplicity of those analytic models, they have provided a useful insight into the problem of transport and mixing in meandering

jet currents and vortex flows. Powerful oceanic currents, such as the Gulf Stream in the North Atlantic and the Kuroshio in the North Pacific, are meandering jets which transport a large amount of heat and release that to the atmosphere strongly affecting climate. They are regions with one of the most intense air-sea heat exchange and the highest eddy kinetic energy level. Transport of water masses across strong jet currents, is important because they separate waters with distinct bio-physico-chemical properties. It may cause heating and freshening of waters with a great impact on the weather and living organisms.

Chaotic mixing and transport in jet and vortex flows have been extensively studied with time-periodic kinematic models (see, e.g., [14–18] and references therein) and with time-periodic dynamical models conserving the potential vorticity (see, e.g., [19–31] and references therein). The problem has been studied as well in laboratory where azimuthal jets with Rossby waves have been produced in rotating tanks [32, 33]. It has been found both numerically and experimentally that fluid is effectively mixed along the jet, but in common opinion a large gradient of the potential vorticity in the central part prevents transport across the jet under realistic values of the Rossby wave amplitudes. The transport barrier was conjectured, based on numerical results [23], to be broken only with so large amplitude values that cannot be reached in real flows. However, in Refs. [26, 27] it has been shown analytically and numerically that chaotic cross-jet transport under appropriate conditions is possible at comparatively small values of the wave amplitudes and, therefore, may occur in geophysical jets. A general method has been elaborated in those papers to detect a core of the transport barrier and find a mechanism of its destruction using the dynamical model of a zonal jet flow with two propagating Rossby waves. The method comprises the identification of a central invariant curve, which is an indicator of existence of the barrier, finding certain resonance conditions for its destruction and detection of cross-jet transport.

The real oceanic flows are not, of course, strictly time-periodic. In aperiodic flows there exist HSPs and HTs as well, but of a transient nature. It is possible to identify aperiodically moving HSPs with stable and unstable effective manifolds [34]. Unlike the manifolds in steady and periodic flows, defined in the infinite time limit, the “effective” manifolds of aperiodic HSPs have a finite lifetime. The point is that they play the same role in organizing oceanic flows as do invariant manifolds in simpler flows. The effective manifolds in course of their life undergo stretching and folding at progressively small scales and intersect each other at homoclinic points in the vicinity of which fluid particles move irregularly. Trajectories of initially close fluid particles diverge rapidly in those regions, and particles from other regions appear there. It is the mechanism for effective transport and mixing of water masses in the ocean. Moreover, stable and unstable effective manifolds constitute Lagrangian transport barriers between different regions, because they are material invariant curves that cannot be crossed by purely advective processes.

The stable and unstable manifolds of influential HSPs are so important because (1) they form a kind of a skeleton in oceanic flows, (2) they partition a flow in dynamically distinct regions, (3) they provide inhomogeneous mixing with spirals, filaments and intrusions which are often visible on satellite images, (4) they are transport barriers separating water masses with different bio-physico-chemical characteristics. Stable manifolds act as repellers for surrounding waters but unstable ones are a kind of attractors. That is why unstable manifolds may be rich in nutrients being oceanic “dining rooms”.

### 1.3 Lagrangian coherent structures

The existence of large-scale quasi-deterministic coherent structures in quasi-random (turbulent) flows has long been recognized (see, e.g., [35]). Before the coherent structures were found, it was a common opinion that turbulent flows are determined only by irregular vortical fluid motion. Although up to now there is no consensus on a strict definition of coherent structures, they can be considered as connected turbulent fluid masses with phase-correlated (i.e., coherent) vorticity over the spatial extent of the shear layer. Thus, turbulence consists of coherent and phase-random (incoherent) motions with the latter ones to be superimposed on the former ones. Lagrangian motion may be strongly influenced by those coherent structures that support distinct regimes in a given turbulent flow. The discovery that turbulent

flows are not fully random but embody orderly organizing structures was a kind of revolution in fluid mechanics.

As to complicated but not totally random flows, including large-scale geophysical ones, it was Haller [34] who proposed a concept of Lagrangian coherent structures (LCS) with the boundaries delineated by distinguished material lines (surfaces) and advected with the flow. To extract these structures, he proposed to compute finite-time Lyapunov exponents (FTLE). The LCS are operationally defined as local extrema of the scalar FTLE field,  $\lambda(x, y)$ , which characterizes the rate of the fluid particle dispersion over a finite-time interval. They are the most influential attracting and repelling hyperbolic material curves in 2D velocity fields. The LCS are Lagrangian because they are invariant material curves consisting of the same fluid particles. They are coherent because they are comparatively long lived and more robust than the other adjacent structures. The LCS are connected with stable and unstable invariant manifolds of HSPs. A tracer patch, chosen nearby any stable manifold, moves in the course of time to the corresponding HSP squeezing along that manifold. After approaching the HSPs, the patch begins to stretch along the corresponding unstable manifold.

The LCS are supposed to be the most repelling and attracting material lines in 2D flows [34]. The spatial distribution of the FTLE values backward and forward in time is an effective way to compute them. A region under study is seeded with a large number of tracers on a grid. The FTLE values are computed by one of the known methods (one of them is described in Sec. 3.2) for all neighboring grid points for a given period of time, typically from a week to a month. Then one plots the spatial distribution of the FTLE coding its values by color. If there were hyperbolic regions in the velocity field in the area for a chosen period of time, then we should get a spatially inhomogeneous FTLE map with “ridges” and “valleys”. A “ridge” is defined as a curve on which the FTLE is locally maximized in the transverse direction [40]. Both the repelling and attracting LCS can be computed by this way. Integrating the advection equations forward in time and computing the FTLE “ridges”, we extract repelling LCS which approximate influential stable manifolds in the area. Expansion in backward time implies contraction in forward time. Therefore, attracting LCS can be computed analogously but in reverse time. They approximate influential unstable manifolds in the area.

A hard work has been done by many people to enlarge the notion of the LCS and invariant manifolds to finite-time realistic flows. In numerous papers (see, e.g., recent introductory review papers [36,37], papers [38–48,55–58] and references therein) the LCS have been shown to be very useful mean to analyze mixing and transport in different seas and oceans. The aim of this paper is not to focus on the LCS but rather to focus on recent studies of transport and mixing in the ocean using Lagrangian indicators which have been introduced to physical oceanography only recently.

## 2 Lagrangian approach to study transport and mixing in the ocean

### 2.1 Transport and mixing in fluids

There are two common approaches in hydrodynamics to study fluid motion, the Eulerian and Lagrangian ones. In the Eulerian approach one is interested in velocities of the flow at given points on a spatial grid. In the Lagrangian one we look for trajectories of water parcels advected by an Eulerian velocity field (3). It is a more convenient approach to study transport and mixing in the ocean, especially the fate and origin of water masses. The velocity field  $\mathbf{v}(\mathbf{r}, t)$  is supposed to be known analytically, numerically or estimated from satellite altimetry data. While in the Eulerian approach we get frozen snapshots of data, Lagrangian diagnostics enable to quantify spatio-time variability of the velocity field. In this review we deal with large-scale horizontal Lagrangian transport and mixing in the ocean. We are interested in water transport on comparatively large scales exceeding 10 km. Transport is advection of the water mass with its conserved properties due to the fluid’s bulk motion.



Advection requires currents and eddies which are vortical currents.

Mixing is a key concept both in hydrodynamics and in dynamical systems theory which can be defined in a strict mathematical sense. Let us consider the basin  $A$  with a circulation where there is a domain  $B$  with a dye occupying at  $t = 0$  the volume  $V(B_0)$ . Let us consider a domain  $C$  in  $A$ . The volume of the dye in the domain  $C$  at time  $t$  is  $V(B_t \cap C)$ , and its concentration in  $C$  is given by the ratio  $V(B_t \cap C)/V(C)$ . The definition of full mixing is that in the course of time in any domain  $C \in A$  we will have the same dye concentration as for the entire domain  $A$ , i.e.,  $V(B_t \cap C)/V(C) - V(B_0)/V(A) \rightarrow 0$  as  $t \rightarrow \infty$ . In dynamical systems theory the full or global mixing is achieved when a small blob of the phase-space fluid is transformed into a long intricate filament occupying all energetically accessible domain in the phase space. The mixing measures are the Lyapunov exponents. In real flows mixing due to flow kinematics is accompanied by molecular diffusion and small-scale turbulence, the processes which can be ignored in large-scale geophysical flows.

Chaotic advection in theory is chaotic mixing in a regular velocity field. In real flows there are inevitable random fluctuations of that field. If they are small as compared to mean regular values, it is reasonable to call the corresponding phenomenon as chaotic advection, because typical geometric structures have similar forms as in purely deterministic flows but become just more fuzzy [59]. Both turbulence and chaotic advection lead to mixing. What is the difference? Chaotic mixing may occur if the velocity field is quasi-coherent in space and quasi-regular in time, but the motion of tracers is irregular on much more smaller scales. In the ocean chaotic mixing produces smooth large-scale features visible sometimes on satellite images of the ocean color as stretched and folded curves. Turbulent mixing may occur if the velocity field is incoherent in space and irregular in time on the same scales as the motion of tracers. It is homogeneous on comparatively large scales.

## 2.2 How to get a velocity field on the sea surface

The impressive progress in the past two decades in satellite monitoring and development of high-resolution numerical models of ocean circulation have opened up new opportunities in physical oceanography. At the websites <http://www.aviso.oceanobs.com>, <http://oceancolor.gsfc.nasa.gov>, <http://www.nodc.noaa.gov> and others one can monitor day by day the sea surface temperature and salinity, concentration of chlorophyll- $\alpha$ , winds at the ocean surface, sea surface height and many other things. Drifter and buoy observations now cover most areas of the world's oceans at sufficient density to map mean currents at one degree resolution (<http://www.aoml.noaa.gov> and <http://www.nodc.noaa.gov>). Systematic and routine satellite measurements of the World Ocean and atmosphere and their rapid interpretation with the help of numerical forecasting models provide not only final products on the present state of the sea but continuous forecasts of its future conditions as well.

The launch of Earth-observing altimeter satellites in the 1990s opened a new era for studying ocean surface circulation. A satellite radar measures precisely the distance from the radar antenna to the ocean surface by computing the round-trip travel time of a microwave signal. Dynamic topography refers to the topography of the sea surface related to the dynamics of its own flow. In hydrostatic equilibrium, the surface of the ocean would have no topography, but due the ocean currents, its maximum dynamic topography is on the order of two meters and are influenced by ocean circulation, temperature and salinity. A clockwise rotation (anticyclone) is found around elevations on the ocean surface in the northern hemisphere and depressions in the southern hemisphere. Conversely, a counterclockwise rotation (cyclone) is found around depressions in the northern hemisphere and elevations in the southern hemisphere. Combined with precise satellite location data, altimetry measurements yield sea-surface heights which, in turn, allow to infer ocean currents under conditions of the geostrophic balance. Away from the surface and bottom layers, horizontal pressure gradients in the ocean almost exactly balance the Coriolis force. The resulting flow is known as geostrophic. The major currents, such as the Gulf Stream, the Kuroshio and the Antarctic Circumpolar Current, are examples of geostrophic currents. Given a streamfunction  $\Psi(x, y, t) = gh/f$ , one gets from (4) the formula connecting surface geostrophic velocities

with surface slope

$$u_{gs} = -\frac{g}{f} \frac{\partial h}{\partial y}, \quad v_{gs} = \frac{g}{f} \frac{\partial h}{\partial x}, \quad (5)$$

where  $g$  is gravity,  $f = 2\Omega \sin \phi$  is the Coriolis parameter,  $\Omega$  is the angular speed of the Earth,  $\phi$  is the latitude and  $h$  is the sea height above a level surface. Daily geostrophic velocities for the world's oceans, provided by the AVISO database (<http://www.aviso.oceanobs.com>), approximate geostrophic ocean currents for horizontal distances exceeding a few tens of kilometers, and for times greater than a few days. The velocity data covers the period from 1992 to the present time with daily data on a  $1/3^\circ$  Mercator grid.

Satellites can observe some processes in the ocean almost everywhere but near the surface only. Research vessels can measure more variables in the depth, but they are too sparse. Numerical models seem to be a useful complementary tool to get a detailed view of the ocean circulation. Realistic velocity fields can be obtained from numerical multi-layered models of regional and global ocean circulation which are able to reproduce adequately many of mesoscale and submesoscale characteristic features of circulation including eddies of various sizes. Those models assimilate satellite sea-surface height and sea-surface temperature and are forced by surface winds and air-sea fluxes to be estimated from the Reanalysis. They provide the velocities at different depths, from a surface layer to the bottom one. Numerical models are not free, of course, of many sources of errors. So, one should accept their outputs with a caution.

## 3 Numerical computation

### 3.1 Options for advection equations

The satellite-derived and numerically generated velocity fields are given as discrete data sets, rather than analytical functions. Moreover, the velocity field in the ocean is only known for finite times. Some numerical algorithms are needed to solve advection equations with such data sets.

Let the velocity field,  $(u_{i,j}, v_{i,j})$ , is given on a 2D grid  $(\lambda_{i,j}, \varphi_{i,j})$ ,  $i = 0, 1, \dots, N_x$ ,  $j = 0, 1, \dots, N_y$ , where  $\lambda_{i,j}$  is the longitude and  $\varphi_{i,j}$  the latitude. We suppose that the grid can be transformed to a rectangular form, i.e., there exist functions,  $X(\lambda, \varphi)$  and  $Y(\lambda, \varphi)$ , such that  $x_{i,j} = X(\lambda_{i,j}, \varphi_{i,j}) = i\Delta x$  and  $y_{i,j} = Y(\lambda_{i,j}, \varphi_{i,j}) = j\Delta y$ , where  $\Delta x$  and  $\Delta y$  are constants. Simply speaking, there exists a coordinate frame where our grid is rectangular. In the simplest case  $(\lambda_{i,j}, \varphi_{i,j})$  is already rectangular. However, it is inconvenient for global fields due to singularities at poles and dependence of the resolution on latitude. The velocities of oceanic currents are usually given in the units of km per day:  $1 \text{ cm/s} = 0.864 \text{ km/day}$ .

There are a few options to write down the advection equations.

1) *Neither velocities nor coordinates are transformed:*

$$\dot{\lambda} = \frac{10800 \cos \varphi}{\pi R} u, \quad \dot{\varphi} = \frac{10800}{\pi R} v, \quad (6)$$

where  $R$  the Earth's radius, latitude and longitude are in geographic minutes, time is in days and  $u$  and  $v$  are in  $\text{km day}^{-1}$ . The coefficient  $\pi R/10800$ , is equal approximately to a nautical mile 1.852 km. *Advantages:* No coordinate transformations, and inputs and outputs are given in geographic coordinates. *Disadvantages:* The calculation of cosine at each step is a time-consuming procedure. Computation of the cell with current coordinates, which one needs for interpolation, is not simple with a nonrectangular grid.

2) *Transformation of linear velocities to angular ones in the right side of advection equations:*

$$\dot{\lambda} = u, \quad \dot{\varphi} = v, \quad (7)$$

where  $u$  and  $v$  are in minutes per second. *Advantages:* The same as in the first method. *Disadvantages:* The same as with nonrectangular grids.

3) *Transformation of coordinates and velocities to a rectangular grid:*

$$\dot{x} = u, \quad \dot{y} = v. \quad (8)$$

*Advantages:* Simple and fast numerical integration. *Disadvantages:* Since we compute in abstract coordinates, it is necessary to transform input and output data.

In the oceanographic examples followed we have used Eqs. 8 because of a simple, unified code that does not depend on the real grid  $(\lambda_{ij}, \varphi_{ij})$ .

Coordinates  $x$  and  $y$  of a passive particle are related with its latitude  $\phi$  and longitude  $\lambda$  in degrees as follows:

$$\lambda = \frac{x}{60}, \quad \phi = \frac{180}{\pi} \arcsin \tanh \left( \frac{\pi}{180} \left( \frac{y}{60} + y_0 \right) \right), \quad y_0 = \frac{180}{\pi} \operatorname{artanh} \sin \left( \frac{\pi}{180} \phi_0 \right), \quad (9)$$

where  $\phi_0 = -82$ . We use the transformation (9) because the AVISO grid is homogeneous in those coordinates. The velocities  $u$  and  $v$  in eq. (8) are expressed via latitudinal  $U_\phi$  and longitudinal  $U_\lambda$  components of the linear velocity  $U$  in cm/s as follows:

$$u = \frac{10800}{\pi R_E \cos \phi} \frac{86400}{100000} U_\lambda \approx \frac{0.466}{\cos \phi} U_\lambda, \quad v = \frac{10800}{\pi R_E \cos \phi} \frac{86400}{100000} U_\phi \approx \frac{0.466}{\cos \phi} U_\phi. \quad (10)$$

The velocity field is given on a grid  $(x_{i,j}, y_{i,j}, t_k)$ . In order to integrate the advection equations, we need to know velocities between the grid points interpolating a given data in space and time. Thus, our numerical algorithm for solving advection equations is as follows.

1. Transformation of coordinates and velocities to a rectangular grid with creating a file with information about the grid (the number and size of steps in space and time) and velocities.
2. A bicubical interpolation in space and an interpolation by third order Lagrangian polynomials in time are used. The velocity components are interpolated independently on each other.
3. The velocities obtained are substituted in Eq. (8) which is integrated with a fourth-order Runge-Kutta scheme with a fixed time step.
4. The outputs are analyzed and then transformed in the geographical coordinates to get images and maps.

### 3.2 Computing finite-time Lyapunov exponents

A general method for computing finite-time Lyapunov exponents (FTLE), which is valid for  $n$ -dimensional vector fields, has been proposed recently [45]. The Lyapunov exponents in this method are computed via singular values of the evolution matrix,  $\sigma_i$ , which obeys the differential matrix equation

$$\dot{G} = JG, \quad (11)$$

with the initial condition  $G(t_0, t_0) = I$ , where  $I$  is the unit matrix. Here  $J$  is Jacobian matrix for the linearized  $n$ -dimensional equations of motion. After a singular-value decomposition of the evolution matrix, one gets the expression for the Lyapunov exponents

$$\lambda_i = \lim_{t \rightarrow \infty} \frac{\ln \sigma_i(t, t_0)}{t - t_0}, \quad n = 1, 2, \dots \quad (12)$$

Quantities

$$\lambda_i(t, t_0) = \frac{\ln \sigma_i(t, t_0)}{t - t_0} \quad (13)$$

are called FTLE which of each is the ratio of the logarithm of the maximal possible stretching in a given direction to a finite time interval  $t - t_0$ .

The formulae above are valid with any  $n$ -dimensional set of nonlinear differential equations. In the two-dimensional case of particle's advection on the ocean surface (4) the singular-value decomposition of the  $2 \times 2$  evolution matrix is as follows:

$$G \equiv \begin{pmatrix} a & b \\ c & d \end{pmatrix} = \begin{pmatrix} \cos \phi_2 & -\sin \phi_2 \\ \sin \phi_2 & \cos \phi_2 \end{pmatrix} \begin{pmatrix} \sigma_1 & 0 \\ 0 & \sigma_2 \end{pmatrix} \begin{pmatrix} \cos \phi_1 & -\sin \phi_1 \\ \sin \phi_1 & \cos \phi_1 \end{pmatrix}. \quad (14)$$



Solution of these four algebraic equations are

$$\begin{aligned}
\sigma_1 &= \frac{\sqrt{(a+d)^2 + (c-b)^2} + \sqrt{(a-d)^2 + (b+c)^2}}{2}, \\
\sigma_2 &= \frac{\sqrt{(a+d)^2 + (c-b)^2} - \sqrt{(a-d)^2 + (b+c)^2}}{2}, \\
\phi_1 &= \frac{\arctan2(c-b, a+d) - \arctan2(c+b, a-d)}{2}, \\
\phi_2 &= \frac{\arctan2(c-b, a+d) + \arctan2(c+b, a-d)}{2},
\end{aligned} \tag{15}$$

where function  $\arctan2$  is defined as

$$\arctan2(y, x) = \begin{cases} \arctan(y/x), & x \geq 0, \\ \arctan(y/x) + \pi, & x < 0. \end{cases} \tag{16}$$

The method described has been applied to study large-scale transport and mixing in different regions in the ocean [45–48, 50–54].

## 4 Elliptic and hyperbolic regions in the ocean

The AVISO altimetric field is provided with a day interval. “Instantaneous” stagnation points in such a field are those points in a fixed day where the AVISO velocity is found to be zero. Their local stability properties are characterized by eigenvalues of the Jacobian matrix of the velocity field. For 2D flows, if the two eigenvalues are real and of opposite sign, then the stagnation point is a HSP. If they are pure imaginary and complex conjugated, then one gets an ESP. The two zero eigenvalues of the Jacobian matrix means the existence of a parabolic stagnation point. The stagnation points are typically moving Eulerian features in a frozen-time velocity field. They are not fluid particle trajectories. The example of the altimetric velocity field in the North Western Pacific is shown in Fig. 2a with overlaid positions of hyperbolic (crosses) and elliptic (triangles) stagnation points. The ESPs are situated mainly in the centers of eddies and allow to identify the latter. The saddle-type HSPs are situated mainly between the eddies or nearby single eddies. They are important because they are features attracting water in one direction and expelling water in the other one.

Stagnation points may undergo bifurcations. Bifurcation theory, among other things, is interested in behavior of fixed points of vector fields as a parameter is varied. In our case time plays the role of the parameter. One may monitor positions of HSPs and ESPs day by day and look for their movement around in the ocean flow. Nothing interesting, besides a rearrangement of the flow, occurs if they do not change their stability type. When they do that, there are, in principle, a few possibilities [60]. In the saddle-node bifurcation two stagnation points, a HSP and a ESP, collide and annihilate each other in the course of time. The opposite process could occur as well: two stagnation points, one HSP and one ESP, are born suddenly. After the collision stagnation points may move apart without changing in number (transcritical bifurcation) or split into three ones (pitchfork bifurcation). In fact, we have observed only saddle-node bifurcations in the altimetric velocity field in the region shown in Fig. 2.

Stable and unstable manifolds of hyperbolic objects can be identified by local and global methods. In the local approach, first of all, one locates positions of HSPs. Then it is necessary to identify the HTs which are situated, as a rule, nearby the HSPs. It can be done by different ways. We prefer to use a HSP as the first guess, placing in a fixed day a few material segments oriented at different angles and computing the FTLE for the particles on those segments. Coordinates of the particles with the maximal FTLE give us approximate position of the HT nearest to that HSP on that day. Then we place the patch with a large number of synthetic particles, centered at the HT position, and evolve it forward in time. It is shown in Figs. 2b and c how the method works in the Oyashio – Kuroshio frontal zone

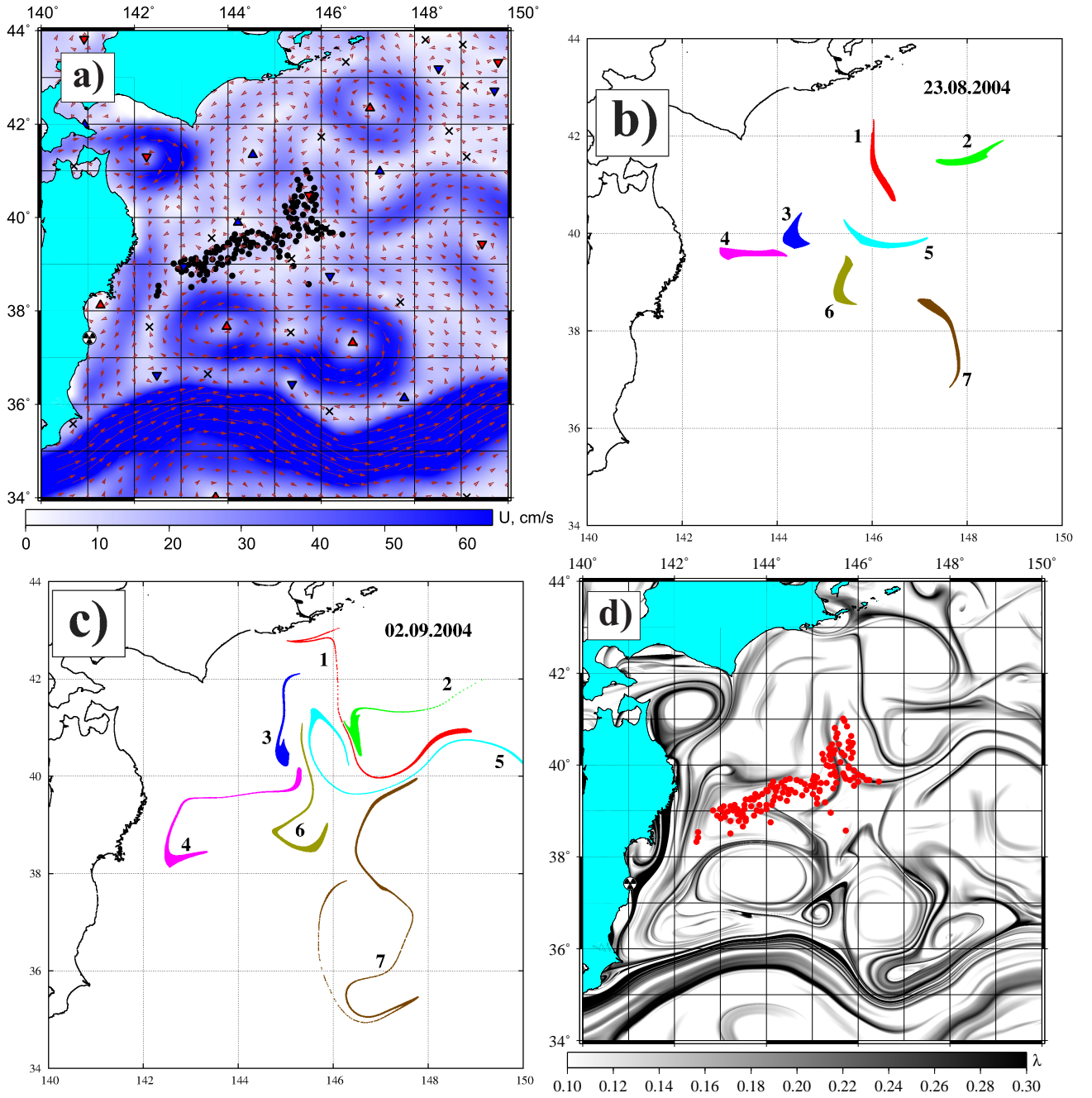


Figure 2: a) The altimetric velocity field in the North Western Pacific on 19 August 2004 with overlaid tuna fishing locations (dots) and elliptic (triangles) and hyperbolic (crosses) “instantaneous” stagnation points. b) and c) Evolution of 7 patches with synthetic particles placed on August, 19, 2004 at 7 HSPs in the region. For two weeks the patches delineate the corresponding unstable manifolds seen as the black ridges on the backward-time FTLE map in d) with  $\lambda$  in days<sup>-1</sup>.

in the northwestern part of the Pacific Ocean to the east off Japan, where the subarctic waters of the cold Oyashio Current encounter the subtropical waters of the warm Kuroshio Current. This region is known to be one of the richest fishery in the world. The jet of the Kuroshio Extension in the south, the two anticyclonic mesoscale eddies to the north of the jet, the Kuroshio ring near the Hokkaido Island with the center at (147°E; 42°4N) and the anticyclonic mesoscale eddy at the traverse of the Tsugaru straight (142°3E; 41°4N) are clearly seen in Fig. 2a. Figures 2b and c show how the corresponding unstable manifolds evolve from 7 tracer patches placed near the 7 HTs.

In the global approach, one seeds the whole area with a large number of synthetic particles and compute the FTLE field which is a commonly used measure of hyperbolicity in oceanic

and atmospheric flows. It has been shown by Haller [34,36] that the curves of local maxima of the FTLE field attributed to initial tracer's positions approximate stable manifolds when computing advection equations forward in time and unstable ones when computing them backward in time (see Sec. 1.3). To compare the results obtained in the local and global approaches, we compute the FTLE field in the same region. Comparing Fig. 2 c with the backward-time FTLE map on 2 September in Fig. 2 d, it is seen that the patches delineate the corresponding ridges on the backward-time FTLE map. The patches nos. 1–5 were chosen in productive waters with comparatively high chlorophyll- $\alpha$  concentration, but in the course of time they have been transformed into narrow filaments to be penetrated into oligotrophic waters, poor with nutrients. The passive marine organisms in those fluid patches are advected along with them into oligotrophic waters attracting fish and marine animals for feeding.

## 5 Lagrangian maps and Lagrangian fronts

The Lyapunov maps provide valuable information on the LCS in oceanic flows. Additional information about the origin, history and fate of water masses can be obtained based on synoptic maps of the Lagrangian indicators measuring some quantities along a parcel trajectory. Among them are vorticity, a distance passed by fluid particles for a given time, absolute,  $D$ , meridional,  $D_y$ , and zonal,  $D_x$ , displacements of particles from their initial positions, the time of residence of fluid particles in a given region, the number of their cyclonic and anticyclonic rotations and others [45,47,48,55]. The absolute displacement is simply the distance between the final,  $(x_f, y_f)$ , and initial,  $(x_0, y_0)$ , positions of advected particles on the Earth sphere with the radius  $R$

$$D \equiv R \operatorname{arccosh}[\sin y_0 \sin y_f + \cos y_0 \cos y_f \cos(x_f - x_0)]. \quad (17)$$

The Lagrangian indicators can be computed by solving advection equations forward and backward in time in order to know the fate and origin of water masses, respectively. They have been shown recently to be useful in quantifying transport of radionuclides in the Northern Pacific after the accident at the Fukushima Nuclear Power Plant [48,52,55] and in identifying the Lagrangian Fronts favorable for fishing grounds [46,48,50].

Satellite-derived geostrophic velocity field on the fixed day, 14 November 2010, is shown in Fig. 3a for the enlarged area in the North Pacific Ocean. The two powerful currents with increased speed values are visible on the map: the Kuroshio and its Extension to the east of the Japan coast and the Alaskan Stream along the Aleut Islands between the Kamchatka and Alaska peninsulas.

In Fig. 3b we show the Lagrangian drift map on 15 May 2011 visualizing the absolute displacements,  $D$ , for 2.25 millions of particles in the North Pacific to be computed backward in time for two weeks in the altimetric AVISO velocity field. The black color means that the corresponding water parcels on the map drifted considerably as compared to the white colored particles. Practically all the region is covered by mesoscale eddies of different sizes and dipole and mushroom-like structures. A few currents, the Kamchatka, the Oyashio and the Californian ones, look like vortex streets with moving mesoscale eddies each of which is surrounded by a black collar which demarcates the boundary separating the eddy's core from the surrounding waters.

Color contrast on the drift maps demarcate boundaries between waters which passed rather different distances before converging. The map in Fig. 3a demonstrates the ocean fronts on the planetary and synoptic scales, including the subarctic frontal zone in the Japan Sea (situated between the Asia continent and Japan) and low-energetic regions, as for example, the Okhotsk Sea (to the north of the Japan Sea) excepting for its southern part between the Sakhalin and Kuril Islands.

The notion of a Lagrangian Front (LF), introduced recently [48,51], is defined as the boundary between waters with different Lagrangian properties. It may be, for example, a physical property, such as temperature, salinity, density, etc. or concentration of chlorophyll- $\alpha$ . Lateral maximal gradients of those properties would indicate on specific oceanic fronts

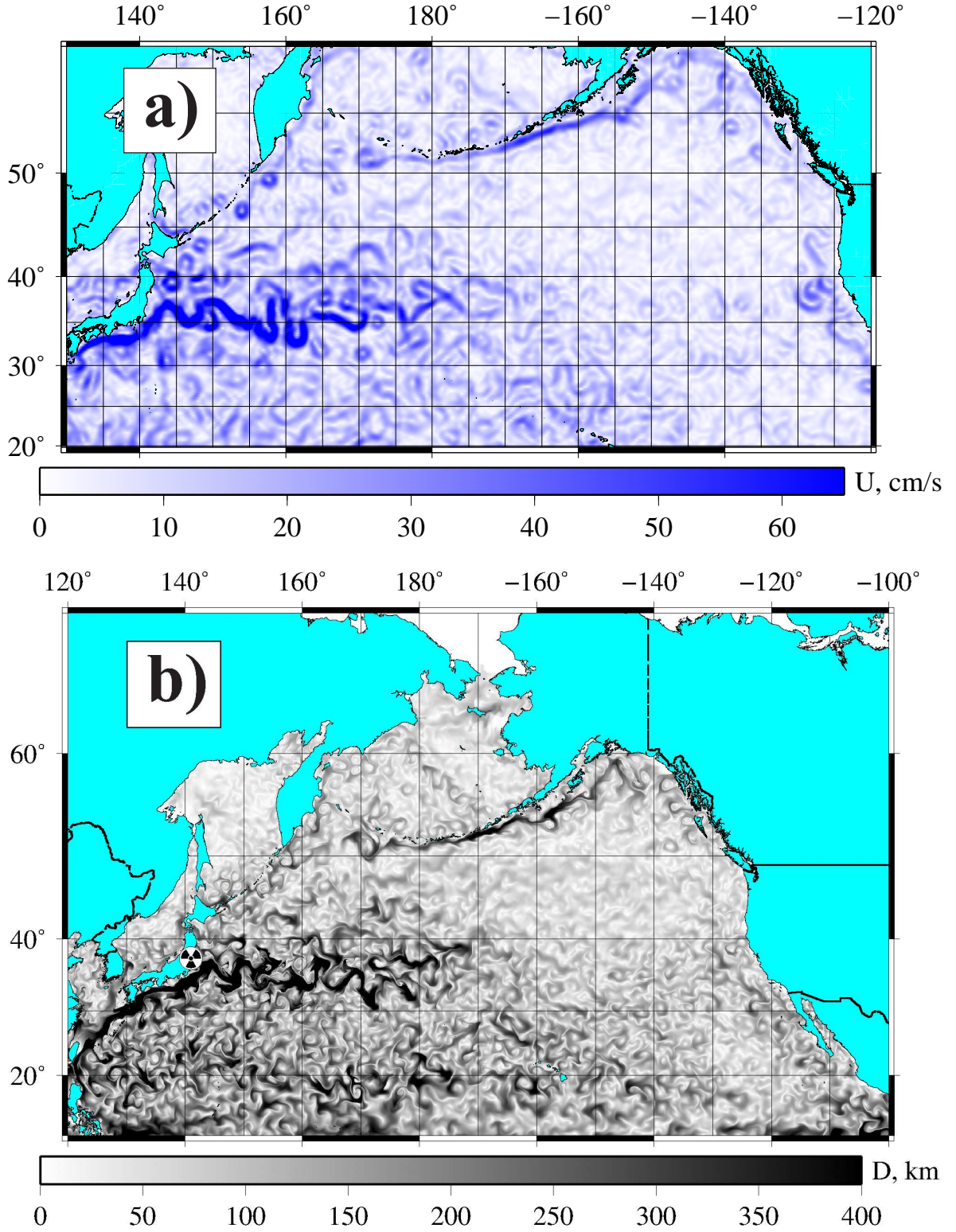


Figure 3: a) Altimetric velocity field on 14 November 2010 ( $U$  in cm/s) and b) the drift map ( $D$  in km) for the North Pacific Ocean on 15 May 2011 computed backward in time for two weeks.

(thermal, salinity, density and chlorophyll ones) which are often connected with each other. However, one may consider more specific Lagrangian indicators such as absolute, meridional or zonal displacements of particles from their initial positions and others. Even in the situation where the water itself is indistinguishable, say, in temperature, and the corresponding sea-surface-temperature image does not show a thermal front there may exist a LF separating waters with the other distinct properties [48,51]. In the satellite era, it becomes possible to monitor common thermal and chlorophyll fronts on the images of sea surface temperature and color, respectively. The definition of the LF given above describes any frontal feature



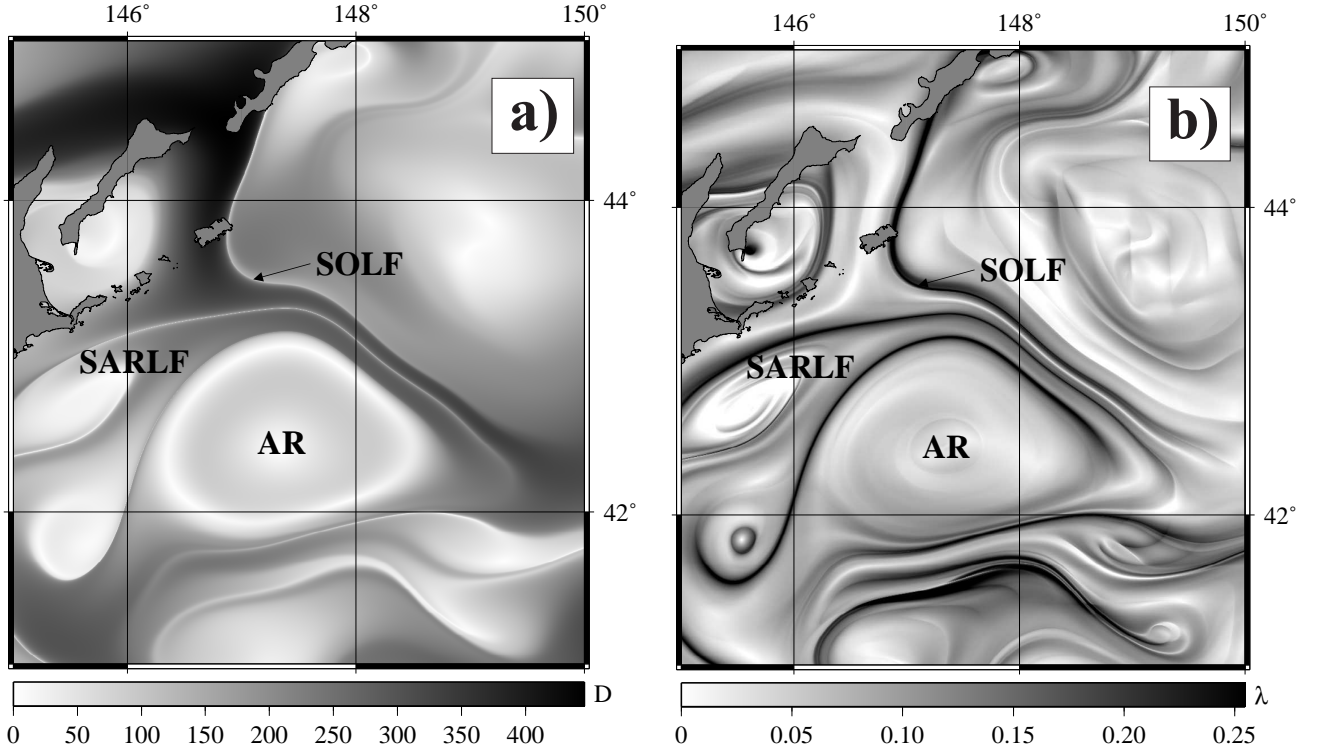


Figure 4: a) Drift and b) Lyapunov maps in the region to the east off the Hokkaido Island and the Kuril Islands on 1 October 2004 computed backward in time for two weeks.

even the one where similar waters from different places converge. For example, one may code by different colors the synthetic particles, that enter into the area under study through different geographical borders. The border between the distinct colors on the corresponding Lagrangian map would be a kind of the LF no matter how different are the properties of convergent waters. However, in practice any LF demarcates convergence of dissimilar waters.

Restricting the area under study, one could resolve fine Lagrangian structures. As an example we plot in Fig. 4 the drift and FTLE maps for the region to the east off the Hokkaido Island and the southern Kuril Islands. A large number of synthetic particles were distributed over that region and integrated backward in time for two weeks to compute the absolute particle's displacements from their initial positions. Coding the particle's displacements by color, one gets information on origin and history of water masses present in the region on a given day. The main regional LFs become visible on the Lagrangian map in Fig. 4a. The SOLF visualizes a convergence of Oyashio waters with the Soya Current flowing from the west through the straits between the islands. The SELF separates the Soya waters from the anticyclonic Kuroshio ring ones with the center at  $(147^\circ.5E; 42^\circ.4N)$ . Each of the LFs can be identified by a narrow white band demarcating the curve of the maximal gradient of  $D$ . White color means that the corresponding particles have experienced very small displacements over two weeks. In order to understand why it is so, we have computed the FTLE in the region. The map in Fig. 4b demonstrates clearly the Kuroshio ring surrounded by black ridges which are known to approximate unstable manifolds of the HTs in the region. The black ridges in Fig. 4b are situated along the corresponding white curves with maximal gradients of  $D$  because motion of particles nearby HPs slows down due to the presence of so-called saddle dynamical traps [16].

It should be stressed that the Lagrangian maps provide a new information on the flow structure and its history that one cannot get looking at altimetric velocity-field daily snapshots or satellite images of sea surface temperature, because the field may (and it really does) fluctuate rather erratically, and the temperature images are not available during cloudy and rainy days. Moreover, those maps enable us to compute “exact” positions of Lagrangian fronts and LCSs in the region.

One of the practical applications of the Lagrangian analysis has been provided recently



in [46, 50]. Using Pacific saury catch and location data of the Russian Fishery Agency for a number of commercial fishery seasons, it was shown statistically that the saury fishing grounds with maximal catches are not randomly distributed over the region but located mainly along the sharp regional LFs where productive cold waters of the Oyashio Current, warmer waters of the southern branch of the Soya Current and waters of warm-core Kuroshio rings converge. Possible biophysical reasons for accumulation of saury schools at some major LFs in the region have been discussed in Refs. [48, 50]. The impact of LCSs on biological organisms has been studied in Refs. [44, 61]. By comparing the seabird satellite positions with computed LCSs locations, it was found in Ref. [44] that a top marine predator, the Great Frigatebird, was able to track the LCSs in the Mozambique Channel identified with the help of the FTLE field. As to another species, they may prefer another ocean features to accumulate at. For example, tuna does not tend to aggregate for feeding at LFs. It is seen in Figs. 2a and d that tuna catch locations are not correlated with the LFs and the LCS in the region. Tuna rather prefers to use mesoscale eddies to move along their boundaries to seek for a food. The recent study [61] of the behavior of tagged elephant seals in the Southern Indian Ocean has shown that they prefer to cross several eddies before staying for intensive searching only in an eddy with large retention time.

Lagrangian fronts can be accurately detected in a given velocity field by computing Lagrangian maps of displacements of synthetic tracers and other Lagrangian indicators. The question is how they correlate with the LCS is open up to now. The Lagrangian indicator, specifying a LF, varies significantly on both sides of the LF. The FTLE values are almost the same on both sides of any ridge in the FTLE field. Local extrema of that field approximate the corresponding LCSs. By definition, any Lagrangian indicator is a function of trajectory, whereas in order to compute the FTLE it is necessary in addition to know the dynamical system as well. Displacement and the other Lagrangian indicators are characteristics of a given fluid particle whereas the Lyapunov exponent is a characteristic of the medium surrounding that particle. We would like to stress the important role of LFs because, in difference from rather abstract geometric objects of an associated dynamical system, like stable and unstable invariant manifolds, they are fronts of real physical quantities that can be, in principle, measured directly.

## 6 Tracking Fukushima-derived radionuclides

The material line technique developed in Ref. [52] is a tool to trace origin, history and fate of water masses. The material line with a large number of particles (markers), crossing a feature under study, evolves backward in time. It is useful sometimes to get as an output tracking Lagrangian maps showing by density plots where the corresponding markers were walking for a given period of time. Placing markers inside a specific mesoscale eddy along the transects where *in-situ* measurements have been carried out before, we can simulate the history and origin of that eddy. It has been done in [52] with Kuroshio rings, large cyclonic and anticyclonic eddies to be pinched off from the meandering Kuroshio Current. The corresponding tracking and drift maps have allowed to document near-surface transport of water masses across the strong Kuroshio Extension jet. That simulation results were supported by tracks of the surface drifters which were deployed in the area [52].

The tracking technique may be useful in planning research vessel cruises in the ocean. Before choosing the track of a planned cruise, it is instructive to make a simulation by initializing backward-in-time evolution of material lines, crossing potentially interesting coherent structures in the region visible on Lagrangian maps. The corresponding tracking maps would help us to know where one could expect, for example, higher or lower concentrations of radionuclides, pollutants or other Lagrangian tracers. This idea has been used in the “Professor Gagarinskiy” cruise to be conducted in the area shown in Fig. 2 from 12 June to 10 July 2012, 15 months after the accident at the Fukushima Nuclear Power Plant on 11 March 2011 [53]. Large amount of water contaminated with radionuclides leaked directly into the ocean. Moreover, the radioactive pollution of the sea after the accident was caused by atmospheric deposition on the ocean surface. Just after the accident radioactive  $^{137}\text{Cs}$  and

$^{134}\text{Cs}$  with 30.07 yrs and 2.07 yrs half-lives, respectively, have been detected over a broad area in the North Pacific. Before March 2011,  $^{137}\text{Cs}$  concentration levels off Japan were  $1 - 2 \text{ Bq m}^{-3} \simeq 0.001 - 0.002 \text{ Bq kg}^{-1}$  while  $^{134}\text{Cs}$  was not detectable. Because of a comparatively short half-life time, any measured concentrations of  $^{134}\text{Cs}$  could only be Fukushima derived.

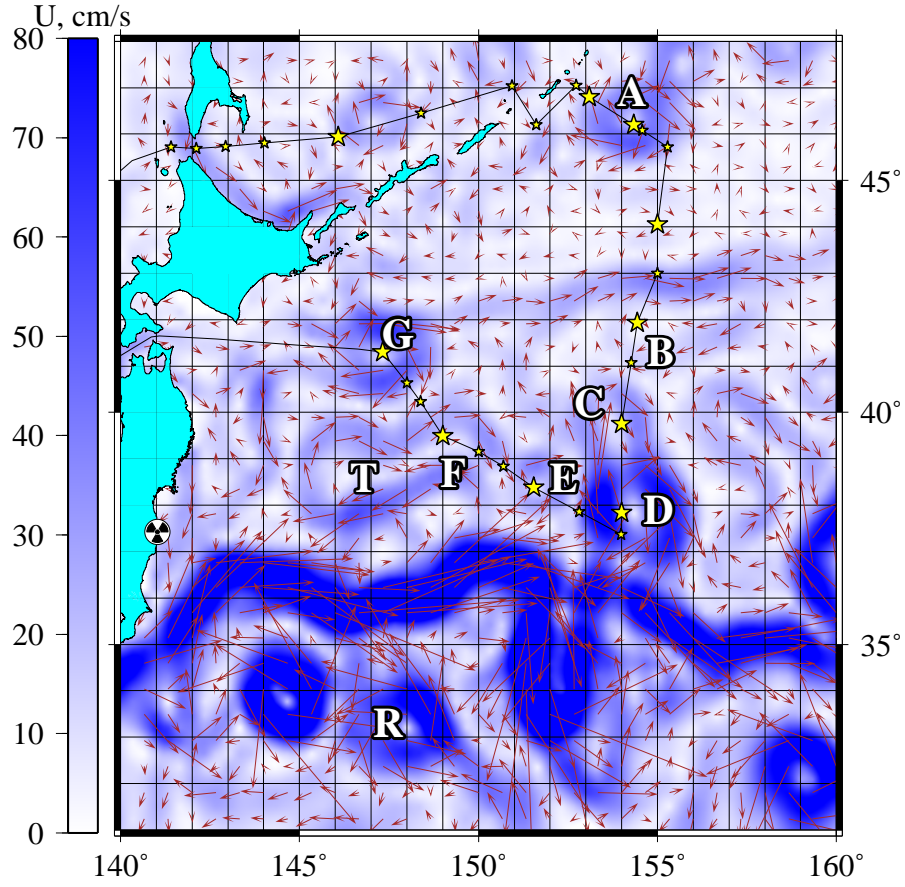


Figure 5: Altimetric velocity field on 28 June 2012 around the Fukushima Nuclear Power Plant (the radioactivity sign) with anticyclonic mesoscale eddies A, B, C, D, E, F and G where seawater samples have been collected in the cruise [53] in the end of June and beginning of July 2012. The ship's track and some sampling stations are shown.

Lagrangian drift and FTLE maps, based on AVISO-provided altimeter velocity fields, have been computed daily and sent by email on the board. The researchers could see daily state of the ocean surface with eddies, strong jets and streamers and plan the cruise track and positions of sampling stations. The frontal Kuroshio – Oyashio zone is populated with mesoscale eddies of different sizes and lifetimes (Fig. 5). The cruise track, shown on the altimetric velocity-field map in Fig. 5, was chosen to cross the anticyclonic eddies A, B, C, D, E, F and G as perspective features for measuring caesium concentration in seawater samples collected at different depth horizons. In simulation, a region around a sampling station was populated with synthetic tracers which have been advected in an altimetric velocity field backward in time beginning from the date of sampling to the day of the accident. Fixing the places on a tracking map, where the corresponding tracers were walking for one month after the accident, the authors [53] were able to estimate by the trace density the probability to detect an increased concentration of Fukushima-derived radionuclides in surface seawater samples at a given station.

The results of simulation have been in a good agreement with *in situ* measurements of  $^{134}\text{Cs}$  and  $^{137}\text{Cs}$ . Four tracking maps are shown in Fig. 6 where density of traces,  $\nu$ , is shown in a logarithmic scale. Station 61 ( $154.4^{\circ}\text{E}; 41.9^{\circ}\text{N}$ ) was located near the elliptic point of the eddy B with the size of  $\simeq 1.5^{\circ}\text{N} \times 1.5^{\circ}\text{E}$ . The highest caesium concentrations,  $21.1 \pm 1.1$  at surface and  $21.6 \pm 0.9 \text{ Bq m}^{-3}$  at 203 m depth, have been observed in seawater samples

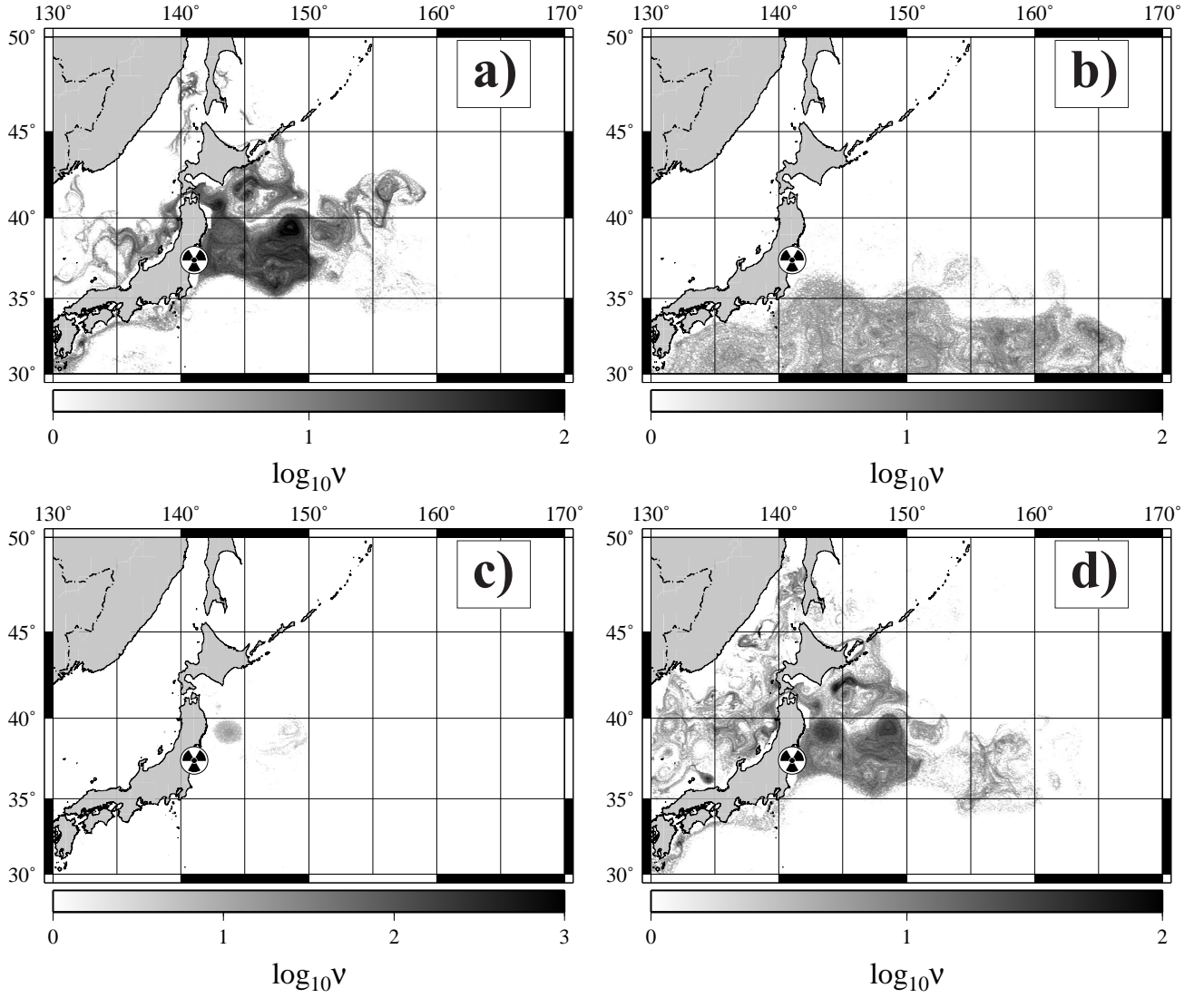


Figure 6: Simulated tracking maps for the synthetic tracers distributed in the centers of the eddies a) B, b) D, c) E and d) G. The maps show by the density plots where those tracers were walking during the month after the accident. The density of traces,  $\nu$ , is in a logarithmic scale.

at that station. It is well agreed with measurements in another cruise [62] to be carried out approximately in the same place at the same time. They detected the concentration of  $^{137}\text{Cs}$  in surface seawater samples to be  $18 \pm 0.7 \text{ Bq m}^{-3}$  at their station B38 located nearby our station 61 and  $17 \pm 0.7 \text{ Bq m}^{-3}$  and  $13 \pm 0.7 \text{ Bq m}^{-3}$  at stations B37 and B39 located inside the eddy B. The tracking map in Fig. 6a shows that synthetic tracers, placed inside a patch around station 61, have visited for the month after the accident the places with presumably high level of contamination. In particular, they have often visited in March and April 2011 the Tohoku eddy (the eddy T in Fig. 5) with the highest levels of caesium concentration to be detected just after the accident [62]. The place of the Tohoku eddy during the month after the accident is clearly seen in Fig. 6c as a circular patch with increased density of points. Tracing out the history of the eddy B [53], it was found that it was born on the southern flank of a zonal eastward jet transporting waters from the eastern coast of the Honshu Island to the open ocean.

The Kuroshio ring D with the size of  $\simeq 3^\circ\text{N} \times 2.5^\circ\text{E}$  was pinched off from a meander of the Kuroshio Extension in the end of May 2012. Until the middle of August it was a free ring to be connected sometimes with the parent jet by an arch. The probability to detect higher concentrations of caesium in its core waters is estimated to be low (see Fig. 6b) because it contains mainly clean Kuroshio waters coming from the south. The concentration of  $^{137}\text{Cs}$ ,  $6.3 \pm 0.4 \text{ Bq m}^{-3}$ , have been detected at station 69 in surface water samples [53]. It

is slightly greater than the background level that can be explained by water exchange with its companion, the eddy C with higher level of radioactivity. The concentrations of  $^{137}\text{Cs}$  in surface seawater samples at Japanese stations B30 located closely to station 69 have been found in [62] to be close to the background level,  $3.6 \pm 0.5$ .

The Kuroshio ring E with the size of  $\simeq 1^\circ N \times 1.5^\circ E$  was pinched off from a meander of the jet on 10 – 12 June 2012 and disappeared in the middle of July. Station 74 ( $151^\circ.5E$ ;  $38^\circ.38N$ ) was located near the elliptic point of that eddy where the increased concentration of  $^{137}\text{Cs}$ ,  $12.3 \pm 0.8 \text{ Bq m}^{-3}$ , has been detected at 307 m depth [53]. A comparatively small number of traces over the whole broad area in Fig. 6c is explained by the history of its core water which have been transported mainly by the Kuroshio from the south and then directed to the east by the Kuroshio Extension. The genesis of the eddy E has shown a presence of the Tohoku eddy waters in its core (see the patch in Fig. 6c).

Station 84 ( $147^\circ.3E$ ;  $41^\circ.3N$ ) was located near the elliptic point of the eddy G with the size of  $\simeq 1^\circ.5N \times 2^\circ E$  situated at the traverse of the Tsugaru Strait between the Honshu and Hokkaido islands. The tracking map for that station in Fig. 6d reveals its close connection with the Tohoku eddy, and, therefore, the probability to detect increased caesium concentrations was expected to be comparatively large. In reality we detected the concentration of  $^{137}\text{Cs}$  at 100 m depth to be  $18 \pm 1.3 \text{ Bq m}^{-3}$ .

*In situ* observations 15 months after the incident were compared with the results of simulation of advection of Fukushima-derived cesium radioisotopes by the AVISO altimetric velocity field. The computed tracking Lagrangian maps were used to reconstruct the history and origin of synthetic tracers imitating measured seawater samples collected in the centers of some mesoscale anticyclonic eddies in the North Western Pacific. Increased Fukushima-derived cesium-isotopes concentrations have been detected in June and July 2012 at sampling stations located in the centers of anticyclonic eddies B and G whose core waters have been demonstrated numerically to visit the areas with presumably high level of contamination just after the accident (Figs. 6a and d). Fast water advection between anticyclonic eddies and convergence of surface water inside eddies make them responsible for spreading and accumulation of cesium rich water.

## 7 Conclusion

The dynamical systems approach provides a new way for describing large-scale chaotic transport and mixing in geophysical flows. It uses tools from dynamical chaos theory to find out and quantify organizing Lagrangian structures in a flow and their impact on large-scale motions. The approach has been firstly applied to simplified analytic models of geophysical flows and then to sophisticated numerical models of ocean circulation. The research in this field is now shifting to study real ocean flows using remote sensing data available to researchers from satellite observations, very high-frequency radars and drifter deployments.

In this article we reviewed briefly some recent advances in applications of the dynamical systems approach to the real ocean with the focus on synoptic maps of some Lagrangian indicators. The basic theoretical ideas from chaotic advection theory have been introduced firstly. Then we described briefly the Lagrangian approach to study transport and mixing in the ocean and some numerical methods used to compute trajectories of fluid particles in satellite-derived velocity fields, Lyapunov exponents and different Lagrangian indicators. The Lagrangian maps, computed with a large number of synthetic tracers in an area under study, have been shown to be useful in identifying the boundaries of different regimes in that area including Lagrangian coherent structures and Lagrangian fronts. We gave a number of illustrations of that approach. As to practical applications, we discussed recent results by the present author and his co-workers on identifying Lagrangian fronts favorable for fishing grounds and on tracking the eddies in the North Pacific with increased concentration of Fukushima-derived radionuclides.

Research in this field has been very active in the last two decades. They seem to be perspective in the future. Among the possible perspective ways of research we would like to mention the following ones. 1) Development of efficient Lagrangian methods for 3D flows.

2) Study of the role of Lagrangian fronts in behavior of marine organisms. 3) Analysis of impact of Lagrangian structures on drifter motion.

## Acknowledgments

I am grateful to Maxim Budyansky, Veniamin Razdobutko and Michael Uleysky for their help in preparing some figures. This work was supported by the Russian Foundation for Basic Research (project nos. 13-05-00099-a and 13-01-12404-ofi-m) and by the Program “Fundamental Problems of Nonlinear Dynamics in Mathematical and Physical Sciences” of the Russian Academy of Sciences.

## References

- [1] V.I. Arnold, C. R. Hebd. Seances Acad. Sci. **261**, 17 (1965).
- [2] M. Henon, C. R. Hebd. Seances Acad. Sci. **262**, 312 (1966).
- [3] H. Aref, J. Fluid Mech. **143**, 1 (1984).
- [4] H. Aref, Phys. Fluids **14**, 1315 (2002).
- [5] J.M. Ottino, *The kinematics of mixing: stretching, chaos, and transport* (Cambridge University Press, Cambridge, 1989).
- [6] M. Budyansky, M. Uleysky, S. Prants, Physica D **195**, 369 (2004).
- [7] M.V. Budyansky, M.Yu. Uleysky, S.V. Prants, Journal of Experimental and Theoretical Physics **99**, 1018 (2004).
- [8] S. Wiggins, Annu. Rev. Fluid Mech. **37**, 295 (2005).
- [9] K.V. Koshel, S.V. Prants, Physics – Uspekhi **49**, 1151 (2006).
- [10] S. Abdullaev, G. Zaslavsky, Usp. Fiz. Nauk **8** 1 (1991).
- [11] D.V. Makarov, M.Yu. Uleysky, S.V. Prants, Chaos **14**, 79 (2004).
- [12] D. Makarov, S. Prants, A. Virovlyansky, G. Zaslavsky, *Ray and wave chaos in ocean acoustics: chaos in waveguides* (World Scientific, Singapore, 2010).
- [13] A.L. Virovlyansky, D.V. Makarov, S.V. Prants, Physics–Uspekhi **55**, 18 (2012).
- [14] R.M Samelson, J. Phys. Oceanogr. **22**, 431 (1992).
- [15] S.V. Prants, M.V. Budyansky, M.Yu. Uleysky, G. M. Zaslavsky, Chaos **16**, 033117 (2006).
- [16] M.Yu. Uleysky, M.V. Budyansky, S.V. Prants, Chaos **17**, 024703 (2007).
- [17] M.Yu. Uleysky, M.V. Budyansky, S.V. Prants, J. Phys. A **41**, 215102 (2008).
- [18] M.V. Budyansky, M.Yu. Uleysky, S.V. Prants, Phys. Rev. E **79**, 056215 (2009).
- [19] R.T. Pierrehumbert, Geophys. Astrophys. Fluid Dyn. **58**, 285 (1991).
- [20] R.T. Pierrehumbert, Chaos, Solit. Fract. **4**, 1091 (1994).
- [21] D. Del-Castillo-Negrete, P.J. Morrison, Phys. Fluids A **5** 948 (1993).
- [22] V.F. Kozlov, K.V. Koshel, Izvestiya Akademii Nauk Fizika Atmosferi i Okeana **35**, 137 (1999).
- [23] I.I. Rypina, M.G. Brown, F.J. Beron-Vera, H. Kozak, M.J. Olascoaga, I.A. Udovychenkov, J. Atmos. Sci. **64**, 3595 (2007).
- [24] K.V. Koshel, M.A. Sokolovskiy, P.A. Davies, Fluid Dyn. Res. **40**, 695 (2008).
- [25] E.A. Ryzhov, K.V. Koshel, D.V. Stepanov, Theor. Comput. Fluid Dyn. **24**, 59 (2010).
- [26] M.Yu. Uleysky, M.V. Budyansky, S.V. Prants, Phys. Rev. E **81**, 017202 (2010).



- [27] M.Yu. Uleysky, M.V. Budyansky, S.V. Prants, Journal of Experimental and Theoretical Physics **111**, 1039 (2010).
- [28] V.V. Zhmur, E.A. Ryzhov, K.V. Koshel, J. Mar. Res. **69**, 435 (2011).
- [29] M.A. Sokolovskiy, K.V. Koshel, X. Carton, Geophys. Astrophys. Fluid Dyn. **105**, 505 (2011).
- [30] E.A. Ryzhov, K.V. Koshel, Izvestiya, Atmospheric and Oceanic Physics **47**, 241 (2011).
- [31] K.V. Koshel, M.A. Sokolovskiy, J. Verron, J. Fluid Mech. **717**, 255 (2013).
- [32] J. Sommeria, S.D. Meyers, H.L. Swinney, Nature **337**, 58 (1989).
- [33] T.H. Solomon, W.J. Holloway, H.L. Swinney, Phys. Fluids A **5**, 1971 (1993).
- [34] G. Haller, Phys. Fluids **14**, 1851 (2002).
- [35] A.K.M.F. Hussain, Phys. Fluids **26**, 2816 (1983).
- [36] T. Peacock, G. Haller, Phys. Today **66** (2), 41 (2013).
- [37] R.M. Samelson, Ann. Rev. Mar. Sci. **5**, 137 (2013).
- [38] E.R. Abraham, M.M. Bowen, Chaos **12**, 373 (2002).
- [39] F. d'Ovidio, V. Fernandez, E. Hernandez-Garcia, C. Lopez, Geophys. Res. Lett. **31**, L17203 (2004).
- [40] S. Shadden, F. Lekien, J.E. Marsden, Physica D **212**, 271 (2005).
- [41] A.D. Jr Kirwan, Prog. Ocean. **70**, 448 (2006).
- [42] Y. Lehahn, F. d'Ovidio, M. Levy, E. Heifetz, J. Geophys. Res. **112**, C08005 (2007).
- [43] F. Beron-Vera, M. Olascoaga, G. Goni, Geophys. Res. Lett. **35**, L12603 (2008).
- [44] E. Tew Kai, V. Rossi, J. Sudre, H. Weimerskirch, C. Lopez, E. Hernandez-Garcia, F. Marsac, V. Garcon, Proc. Nat. Ac. Sci. USA **106**, 8245 (2009).
- [45] S.V. Prants, M.V. Budyansky, V.I. Ponomarev, M.Yu. Uleysky, Ocean modelling **38**, 114 (2011).
- [46] S.V. Prants, M.Yu. Uleysky, M.V. Budyansky, Doklady Earth Sciences **447**, 1269 (2012).
- [47] S.V. Prants, V.I. Ponomarev, M.V. Budyansky, M.Yu. Uleysky, P.A. Fyman, Izvestiya, Atmospheric and Oceanic Physics **49**, 82 (2013).
- [48] S.V. Prants, Physica Scripta **87**, 038115 (2013).
- [49] S.V. Prants, A.G. Andreev, M.V. Budyansky, M.Yu. Uleysky. Ocean Modelling **72**, 143 (2013).
- [50] S.V. Prants, M.V. Budyansky, M.Yu. Uleysky, Deep Sea Res. I **90**, 27 (2014).
- [51] S.V. Prants, M.V. Budyansky, M.Yu. Uleysky, Izvestiya, Atmospheric and Oceanic Physics **50**, 284 (2014).
- [52] S.V. Prants, M.V. Budyansky, M.Yu. Uleysky, Nonlinear Proc. Geophys. **21**, 279 (2014).
- [53] M.V. Budyansky, V.A. Goryachev, D.D. Kaplunenko, V.B. Lobanov, S.V. Prants, A.F. Sergeev, N.V. Shlyk, M.Yu. Uleysky, Deep Sea Res. I (in press).
- [54] S.V. Prants, A.G. Andreev, M.Yu. Uleysky, M.V. Budyansky. Ocean Dynamics **64**, 771 (2014).
- [55] S.V. Prants, M.Yu. Uleysky, M.V. Budyansky, Doklady Earth Sciences **439**, 1179 (2011).
- [56] F. Huhn F, A. von Kameke, V. Perez Munuzuri, M.J. Olascoaga, F.J. Beron-Vera, Geophys. Res. Lett. **39**, L06602 (2012).
- [57] J.H. Bettencourt, C. Lopez, E. Hernandez-Garcia, Ocean Modelling **51**, 73 (2012).
- [58] F.J. Beron-Vera, Y. Wang, M.J. Olascoaga, G.J. Goni, G. Haller, J. Phys. Oceanogr. **43**, 1426 (2013).

- [59] D.V. Makarov, M.Yu. Uleysky, M.V Budyansky, S.V. Prants, Phys. Rev. E **73**, 066210 (2006).
- [60] A.M. Mancho, Des Small, S. Wiggins, Phys. Rep. **437**, 55 (2006).
- [61] F. d'Ovidio, S. de Monti, A.D. Penna, C. Cotte, C. Guinet, J. Phys. A **46**, 254023 (2013).
- [62] H. Kaeriyama, et al, Biogeosciences **10**, 4287 (2013).